

Article

Modeling and NVH Analysis of a Full Engine Dynamic Model with Valve Train System

Xu Zheng , Xuan Luo , Yi Qiu * and Zhiyong Hao

College of Energy Engineering, Zhejiang University, Hangzhou 310027, China; zhengxu@zju.edu.cn (X.Z.); 3090100538@zju.edu.cn (X.L.); haozy@zju.edu.cn (Z.H.)

* Correspondence: yiqiu@zju.edu.cn; Tel.: +86-057-87953286

Received: 6 July 2020; Accepted: 23 July 2020; Published: 27 July 2020



Abstract: The valve train system is an important source of vibration and noise in an engine. An in-depth study on the dynamic model of the valve train is helpful in understanding the dynamic characteristics of the valve train and improving the prediction accuracy of vibration and noise. In the traditional approaches of the dynamic analyses, the simulations of the valve train system and the engine are carried out separately. The disadvantages of these uncoupled approaches are that the impact of the cylinder head deformation to the valve train and the support and constraints of the valve train on the cylinder head are not taken into consideration. In this study, a full engine dynamic model coupled with a valve train system is established and a dynamic simulation and noise vibration harshness (NVH) analysis are carried out. In the coupled approach, the valve train system is simulated simultaneously with the engine, and the complexity of the model has been greatly increased. Compared with the uncoupled approach, more detailed dynamic results of the valve train can be presented, and the subsequent predictions of vibration and noise can also be more accurate. The acoustic results show that the difference from the experimental sound power level is reduced from 1.8 dB(A) to 0.9 dB(A) after applying the coupled approach.

Keywords: valve train; dynamics; coupled approach; NVH

1. Introduction

The valve train system is one of the important sources of vibration and noise in an internal combustion engine. For an ideal valve train system, on the one hand, the valve should be opened and closed as quickly as possible to improve the ventilation efficiency; on the other hand, each component should be operated smoothly to avoid the occurrence of jump, bounce, and overload, causing failures or noise vibration harshness (NVH) problems. The valve train dynamic model is used to simulate the motions and forces of the valve, spring, rocker, camshaft, hydraulic lash adjuster (HLA), and other parts during the actual operation of the engine. Therefore, the establishment of a comprehensive and accurate dynamic model is of great significance for studying dynamic problems and predicting the vibration and noise.

The earliest valve train dynamic model is a single degree of freedom (DoF) model proposed by W. M. Dudley [1]. All the valve train parts, including the valve, washer, lock, and part of the spring, are simplified as an equivalent mass. The model is too simple to predict the valve motion accurately. N. S. Eiss established a valve train dynamic model with two DoFs, and demonstrated how the parameters of the model were selected to give the minimum vibration amplitude [2]. Since the 1980s, it has become easier to solve complex multivariate dynamic equations with the assistance of the modern computer. Models with distributed masses take elastic deformations into consideration, and more factors can be studied. C. Chan formulated a 6-DoF dynamic model to predict the forces and the motions of the end-pivot rocker-arm cam system components [3]. S. Seidlitz built a valve train

dynamic model with 21 DoFs to simulate the single valve train system of an overhead valve (OHV) engine [4]. K. Nagaya studied the jump and bounce phenomena of a driven valve system based on a multiple-DoF dynamic model [5]. A. P. Pisano and F. Freudenstein considered the valve spring as a continuous flexible body. The valve spring was modeled as a distributed parameter system governed by the damped wave equation [6]. W. Lassaad et al. investigated the nonlinear dynamic behavior of a cam mechanism with an oscillating roller follower in the presence of defects by a multiple-DoF lumped-mass model with two nonlinear hertzian contacts [7]. J. Guo et al. proposed a mode matching method (MMM) for valve train components in a multiple-DoF dynamic model. The amount of lumped masses for each flexible component was determined based on its natural frequencies and the considered frequency range [8]. C. J. Zhou et al. proposed an enhanced flexible dynamic model for a valve train with clearance and multi-directional deformations and verified the model with experiments. They investigated the effects of valve clearance and cam rotation speed on the contact force, acceleration, and dynamic transmission error [9].

Based on various multiple-DoF valve train dynamic models, each body and joint in the system has been modeled and analyzed in detail. However, all the above approaches just consider the valve train system as an independent system, ignoring the interaction between the valve train system and other parts of the engine, which will affect the accuracy of the dynamic modelling. In this paper, the dynamic models of the valve train system and other parts of the engine are combined into one model, forming a completed coupled engine dynamic model with the valve train system. In this coupled approach, not only the internal interactions of the valve train system, but also the external interactions between the valve train system and other parts of the engine are taken into consideration. For a valve train system in the form of end-pivot rocker arm with roller finger follower, the external interactions act not only on valves, springs, and bearings, but also on HLAs. Based on the full engine model coupled with valve train system, the dynamic simulation is performed, and the vibration and noise characteristics are predicted.

2. Theory

The dynamic model is based on the floating frame of reference (FFoR) formulation [10]. For large-scale displacement, the Lagrangian formulation is employed. The small elastic deformations are considered relative to a local frame of reference, while this local frame of reference undergoes large motions with respect to a fixed global frame of reference [11]. Each discrete mass of the model is governed by Newton–Euler equation of motion. The analysis is performed by the implicit integration method (Newmark) in the time domain [12].

Considering the complexity of the engine model, it needs to be greatly simplified, as shown in Figure 1. Besides the parametric and lumped-mass models, the finite element method (FEM) is commonly used for simplifications. An accurate NVH analysis requires that the element size should not be too small. The lower limit of the wavelength is calculated according to the upper limit of the analysis frequency, and then the density of the element is determined. Due to the complexity of the engine structure of the components, there are hundreds of thousands of elements in the engine FEM model. In order to reduce the DoFs and modes of the matrices to an acceptable level for calculation, component mode synthesis (CMS) is applied in the condensation of the FEM models [13]. Only a few main modes of substructures are retained in the condensed FEM models and participate in the calculations of the equations of motion.

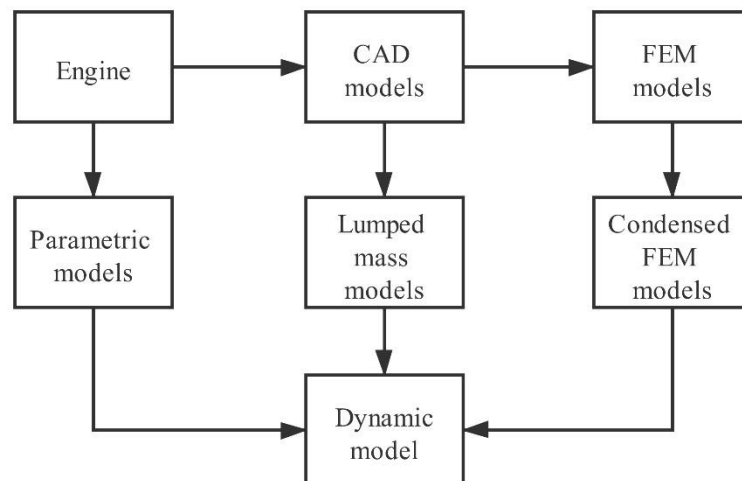


Figure 1. Simplification process of the engine model.

The schematic representation of the FFor is shown in Figure 2. $e^T = (e_1, e_2, e_3)$ and $b^T = (b_1, b_2, b_3)$ denote the global coordinate system and the local coordinate system, respectively.

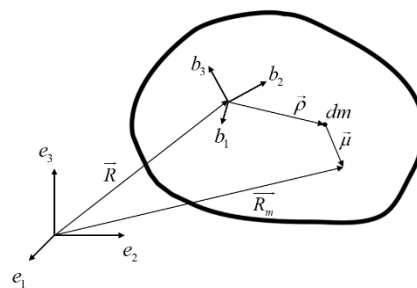


Figure 2. Schematic representation of the floating frame of reference (FFoR) approach.

\vec{R} denotes the global body position vector, $\vec{\rho}$ denotes the global coordinate system initial position vector, and $\vec{\mu}$ denotes the elastic displacement of the node dm . The reference position vector can be written as:

$$\vec{R}_m = \vec{R} + \vec{\rho} + \vec{\mu} = e^T \hat{R} + b^T \hat{\rho} + b^T \hat{\mu}, \tag{1}$$

where \hat{R} , $\hat{\rho}$, $\hat{\mu}$ are the component matrices of \vec{R} , $\vec{\rho}$, $\vec{\mu}$.

The elastic displacement expanded in modal coordinates can be written as:

$$\vec{\mu} = b^T \Phi \varepsilon, \tag{2}$$

where Φ is the eigenvector; ε is the modal participation factor.

The Lagrange equation is defined as:

$$L = T - U, \tag{3}$$

where T is the kinetic energy; U is the potential energy.

$$T = \frac{1}{2} \int |\vec{v}_m| |\vec{v}_m| dm = \frac{1}{2} \int \left| \frac{d\vec{R}_m}{dt} \right| \left| \frac{d\vec{R}_m}{dt} \right| dm, \tag{4}$$

$$U = \frac{1}{2} \varepsilon^T \Lambda \varepsilon, \tag{5}$$

where \vec{v}_m is the velocity vector of dm ; Λ is the diagonal matrix of the natural frequencies, defined as $\Lambda = \text{diag}[\lambda_1^2 \ \lambda_2^2 \ \dots]$.

The basic dynamic equations in the FFor can be obtained by substituting Equations (4) and (5) into the Lagrange equation:

$$\frac{d}{dt} \frac{\partial L}{\partial \dot{q}} - \frac{\partial L}{\partial q} = Q_q, \tag{6}$$

where Q_q denotes generalized force, and q denotes generalized coordinate.

Based on the Newton–Euler method, the governing equation of motion in the multi-body system can be expressed as:

$$M \cdot \ddot{q} + C \cdot \dot{q} + K \cdot q = f_e + f_l + f_c, \tag{7}$$

where M , C , and K denote mass, damping, and stiffness matrix; q denotes the vector of the system generalized coordinates; f_e denotes the excitation loads; f_l denotes the external loads; f_c denotes the constraint forces.

Both the uncoupled and coupled approach adopted the classical Newton–Euler equation, but the difference is the consideration of the valve train system. In the uncoupled approach, the forces to the engine from the valve train are considered as external loads in the term f_l . In the coupled approach, the components of the valve train system are merged in the matrices and vectors at the left-hand side of the equation.

The condensation approach is based on the Craig–Bampton method, which is an improved fixed-interface CMS method [14]. The main modes of each substructure are retained, and the DoFs of the substructures are reduced. The omitted internal displacements r_i are determined by:

$$\begin{bmatrix} r_i \\ r_e \end{bmatrix} = \begin{bmatrix} B & \Phi \\ I & 0 \end{bmatrix} \begin{bmatrix} r_e \\ \varepsilon \end{bmatrix}, \tag{8}$$

where r_e is the external displacements, B is the static modes, Φ is the component modes (eigenvectors), and ε is the modal participation factor.

3. Modeling and Analysis

3.1. Engine Basic Parameters

The engine is a four-cylinder turbocharged gasoline engine, the layout of the valve train is a double overhead camshaft (DOHC), with an end-pivot rocker arm with a roller finger follower and hydraulic lash adjuster, which is in the most common form in passenger cars. The basic specification of the engine is shown in Table 1.

Table 1. Specification of the engine.

Engine type	Four cylinders four strokes gasoline engine
Intake type	Turbocharged
Displacement	1798 cc
Bore	82.5 mm
Stroke	84.2 mm
Max power	120 kW@5500 rpm
Max torque	250 Nm@1500–4500 rpm
Balance	Double balancing shaft
	DOHC
Valve train	End-pivot rocker arm (roller finger follower) HLA

3.2. FEM Models

Based on three-dimensional digital models of the engine main components provided by the manufacturer, the FEM models of crankshaft, block, cylinder head, cylinder head cover, timing cover, oil pan, intake manifold, and exhaust system are established, as shown in Figure 3. Given the fact that the crankshaft has a regular and symmetrical structure, the first order hexahedral elements are adopted in the FEM model of the crankshaft. However, other components with many fillets, bolt holes, and oil channels are complex; therefore, second order tetrahedral elements are adopted in the FEM models of the rest components. The parameters of the FEM models are shown in Table 2.

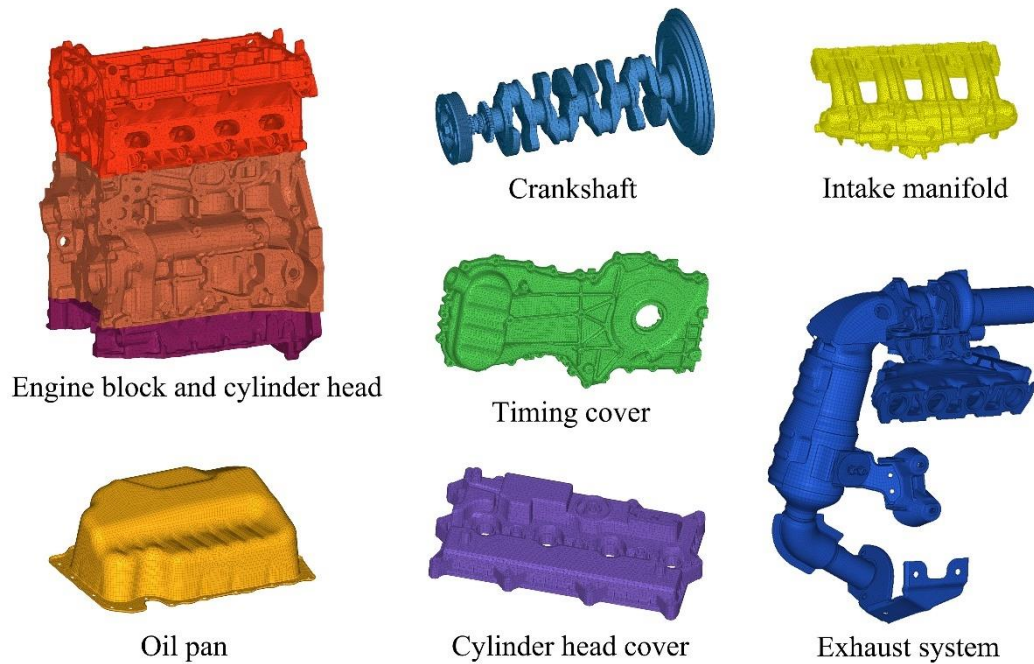


Figure 3. Finite element method (FEM) models of the components.

Table 2. Specification of the engine components.

	Elements	Material	Density (g/cm ³)	Young's Modulus (MPa)	Poisson's Ratio
Crankshaft	93,196	Steel	7.85	210,000	0.30
Oil pan	9043				
Block	269,359	Cast iron	7.30	110,000	0.30
Cylinder head	139,218	Aluminum alloy	2.73	76,550	0.34
Timing cover	91,996				
Cylinder head cover	64,609	Polypropylene	1.40	3150	0.35
Intake manifold	166,391	Polyamide	1.50	1800	0.30
Exhaust system	98,330	Cast iron	7.80	191,000	0.30

The natural frequencies and mode shapes of the main components are measured by the experimental free modal analysis through the Lanczos algorithm and the multi-input single-output (MISO) hammering method [15]. As shown in Figure 4, the components are hung on flexible ropes, a hammer of type PCB 086C03 is used to excite the structures, and an acceleration sensor of type PCB 356A16 is glued to the structures to acquire the vibration signals. The hammer and acceleration sensor are connected to the LMS SCADAS data acquisition front-end, and the signal acquisition and analysis software is LMS Test.Lab.



Figure 4. Modal experiments of components.

The first five modal frequencies of the simulations and measurements are listed in Table 3. Comparing with the experimental results of the components, the errors of the simulation results are within plus or minus 6%, and the mode shape of each component is consistent with the corresponding experimental results. The accuracies of the FEM models of main components are verified, and the FEM models can be used in the following simulations.

Table 3. Modal frequencies of components: comparison of the results from the simulation and measurement.

Components	Order	Simulation/Hz	Measurement/Hz	Error
Engine block (up) and cylinder head	1	545.5	543.6	0.3%
	2	987.3	1042.0	−5.2%
	3	1368.2	1435.9	−4.7%
	4	1455.3	1488.6	−2.2%
	5	1635.9	1673.8	−2.3%
Engine block (low)	1	327.5	309.8	5.7%
	2	793.3	790.9	0.3%
	3	940.5	969.9	−3.0%
	4	1182.8	1145.3	3.3%
	5	1461.8	1385.9	5.5%
Crankshaft	1	406.5	309.6	4.1%
	2	553.5	529.8	4.4%
	3	907.9	881.0	3.1%
	4	950.9	920.9	3.3%
	5	961.6	923.3	4.2%

Table 3. Cont.

Components	Order	Simulation/Hz	Measurement/Hz	Error
Cylinder head cover	1	128.5	133.2	−3.5%
	2	204.1	201.7	1.2%
	3	348.6	346.6	0.6%
	4	386.6	401.1	3.6%
	5	439.6	435.8	0.9%
Timing cover	1	197.6	194.3	1.7%
	2	255.6	250.6	2.0%
	3	539.4	531.5	1.5%
	4	692.3	678.9	2.0%
	5	812.9	804.1	1.1%
Oil pan	1	193.4	197.7	−2.2%
	2	323.1	329.5	−1.7%
	3	502.7	490.9	2.4%
	4	572.0	578.1	−1.1%
	5	775.8	807.4	−3.9%

3.3. Multi-Body Dynamic Model

Based on the actual structures and connections of the engine, a simplified multi-body dynamic model is established, as shown in Figure 5. The excitation of the model comes from the pressure in each cylinder. The pressure forces act downward on the pistons and upward on the cylinder head and valves (omitted in Figure 5). The moving parts of the engine include pistons, conrods, crankshaft, valve train, and balance shafts. The forces from the moving parts act on the structures through joints, including liners, bearings, and seats. The structure bodies of the engine include a cylinder block, cylinder head, cylinder head cover, intake manifold, exhaust system, timing cover, and oil pan.

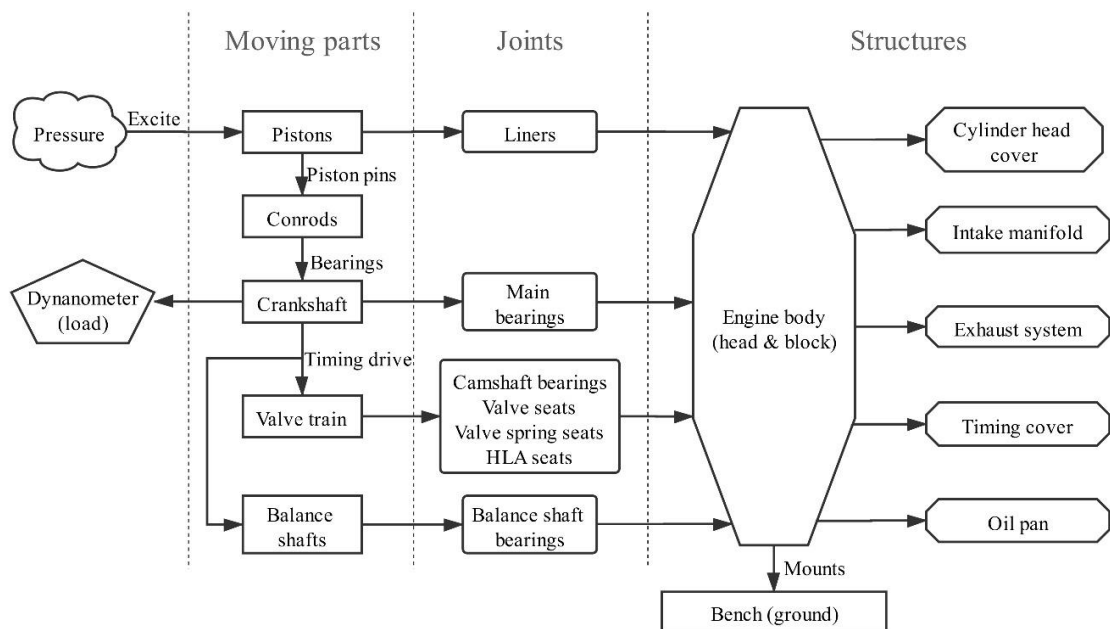


Figure 5. Schematic diagram of the engine model structure.

The conrod is simplified as a beam element, and the mass is distributed to the big end and the small end as lumped mass points. The piston–liner interaction relationship is simplified as a joint with a spring and a damper, as shown in Figure 6. The piston with a piston ring and piston pin is simplified to a mass point which is connected to the points on the liner thrust side (TS) and anti-thrust side (ATS). Each point-to-point connection consists of a linear spring and a damper.

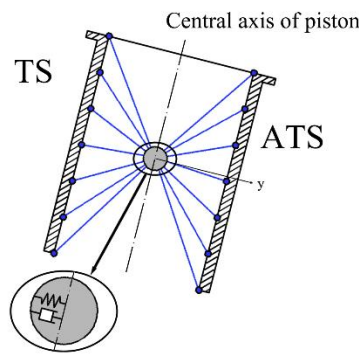


Figure 6. Simplified piston–liner interaction model.

Since the piston’s second-order motion will cause a shift in the piston’s center of mass, the force in the y direction of the piston can be calculated by the following formula:

$$F_p = -k\Delta u_y - c\Delta \dot{u}_y, \tag{9}$$

where k is the equivalent spring stiffness, c is the equivalent damping, Δu_y is the piston’s displacement in the y direction, and $\Delta \dot{u}_y$ is the component of the piston velocity projected in the y direction.

The interaction relationship between the conrod big end and the crank pin is simplified as a point-to-point joint with a non-linear spring and a non-linear damper.

In local coordinates, the bearing force can be calculated as:

$$F_b = k_0 \left(\frac{k_b}{k_0} \right)^{\frac{|\Delta u_{ij}|}{u_0}} \Delta u_{ij} + c_0 \left(\frac{c_b}{c_0} \right)^{\frac{|\Delta u_{ij}|}{u_0}} \Delta \dot{u}_{ij}, \tag{10}$$

where Δu_{ij} is the displacement vector from the center of the conrod big end to the center of the crank pin, k_0 and c_0 are the equivalent stiffness and damping when $|\Delta u_{ij}| = 0$, k_b and c_b are the equivalent stiffness and damping corresponding to Δu_{ij} , and u_0 is the bearing radial clearance.

The joint connecting the main bearing and the main journal is very important in transmitting the load from the crankshaft to the engine block, which is significant to the vibration and acoustic calculation. Therefore, the nonlinear spring and damper (NONL) model is used for the main joint, which is more precise and detailed.

Considering that the oil film only transmits pressure but not tension, only a part of the oil film is compressed when offset at the center of the main journal. As shown in Figure 7, the compressed oil film accounts for approximately 1/3 of the entire bearing (120 degrees).

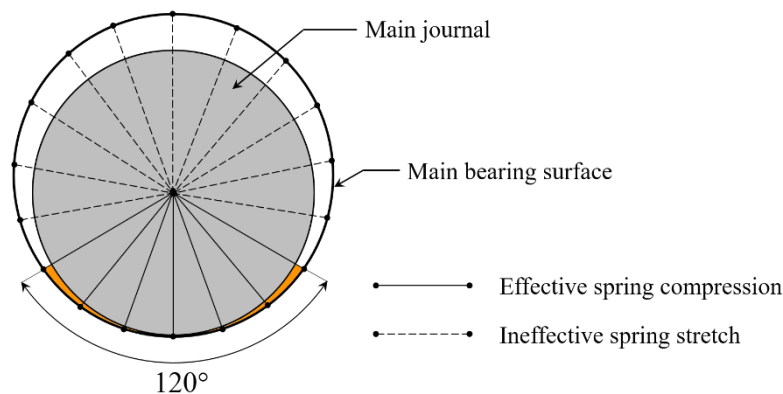


Figure 7. Simplified main journal–main bearing interaction model.

Each line in Figure 7 represents a set of spring and damper. Considering the oil leakage at both ends of the main bearing, the oil film pressure should be parabolic in the axial direction. The stiffness of each spring is defined as:

$$k_{MB} = \frac{F_{\max MB}}{\mu_{0MB} \cdot r} \cdot A, \tag{11}$$

where $F_{\max MB}$ is the maximum main bearing pressure, which can be obtained through the theoretical calculation according to the pressure curve in the cylinder; μ_{0MB} is the radius clearance of the main bearing; r is the number of all the effective compression springs in the bearing; A is the correction factor, $A = 1.5 \sim 3.0$.

The loads of the multi-body dynamic model come from the in-cylinder pressure, the piston slap, and the valve train system.

In-cylinder mixed gas combustion produces high pressure periodically. The pressure is imposed to the piston downward and to the bottom of the cylinder head upward. The measured in-cylinder pressure at 2500 rpm under the wide open throttle (WOT) condition is shown in Figure 8. Under this working condition, the engine outputs the maximum torque at a medium rotation speed, which is relatively frequently used when accelerating. The piston reaches the top dead center (TDC) on the compression stroke when the crank angle is at zero degrees.

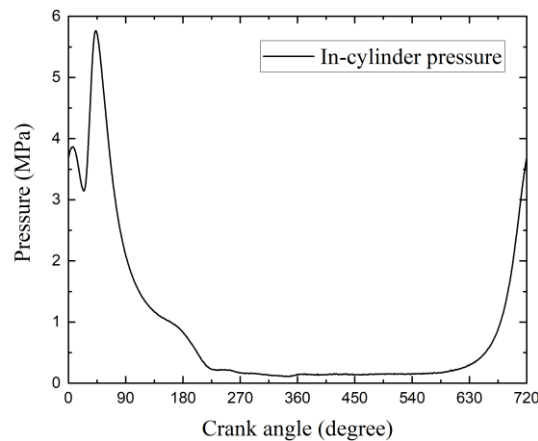


Figure 8. In-cylinder pressure at 2500 rpm under the wide open throttle (WOT) condition.

The load of the in-cylinder pressure is transmitted to the crankshaft through the piston-linkage mechanism, as shown in Figure 9. F_P is the downward force of the in-cylinder pressure on the piston. The conrod force F_C transmitting along the conrod is divided into the radial component F_R and the tangential component F_T .

$$\begin{aligned} F_R &= F_C \cos(\alpha + \beta) = F_P \frac{\cos(\alpha + \beta)}{\cos \beta} \\ F_T &= F_C \sin(\alpha + \beta) = F_P \frac{\sin(\alpha + \beta)}{\cos \beta} \end{aligned} \tag{12}$$

where α is the angle between F_R and F_P , and β is the angle between F_C and F_P .

Due to the existence of the cylinder clearance, the piston has a lateral translation and a rotation around the piston pin during the stroke. The piston lateral force at different height points on the liner TS and ATS is calculated based on the piston dynamic model, then the piston slap excitation to the cylinder liner is obtained. For example, the load of cylinder 1# piston-liner contact force is calculated and shown in Figure 10.

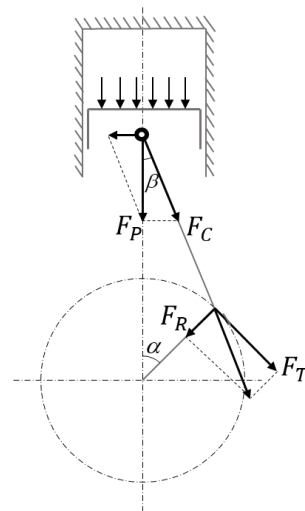


Figure 9. The force transmitting through the conrod.

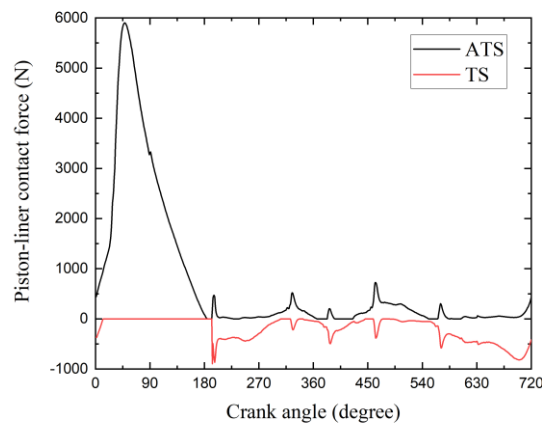


Figure 10. The load of cylinder 1# piston-liner contact force.

3.4. Valve Train System Model

In the uncoupled approach, the dynamic calculation of the valve train system and the dynamic calculation of the engine are carried out separately. The valve train dynamic model is built and calculated independently from the engine; the force results of the joints between the valve train and the engine are loaded onto the engine dynamic model. The disadvantages of the approach are that the impact of the cylinder head deformation to the valve train and the support and constraints of the valve train on the cylinder head are not taken into consideration. The crank speed fluctuation is also neglected or pre-set. In fact, there are important interactions between the valve train and the cylinder head which have significant impacts on the precision of vibration calculation and noise prediction.

In the proposed coupled approach, the dynamic models of the valve train and the engine are combined into one model, forming a full engine dynamic model with the valve train. In this model, the dynamic process between the valve train and the engine is fully analyzed, and the engine dynamic results including the valve train are obtained. The challenge of the coupled approach is the reduced efficiency and solver stability due to the increased complexity of the model. The schematic diagram of differences between the uncoupled and coupled approach is shown in Figure 11.

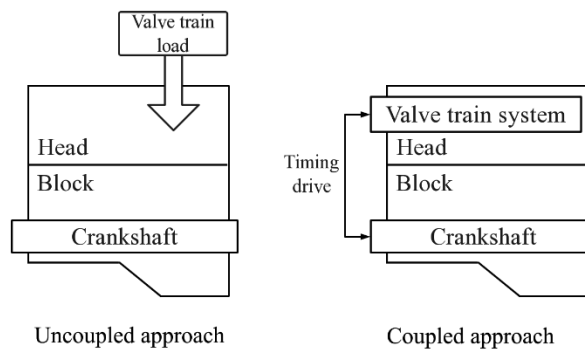


Figure 11. Differences between the uncoupled and coupled approach.

The valve train system model consists of two camshafts with variable valve timing (VVT) phasers, eight single intake valve trains, and eight single exhaust valve trains. The valve train type of the engine is the end-pivot rocker arm overhead camshaft (OHC), as shown in Figure 12. The topology of the valve train system is shown in Figure 13.

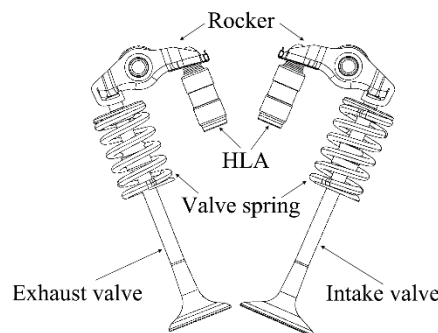


Figure 12. The structure of the intake and exhaust single valve train (SVT) system.

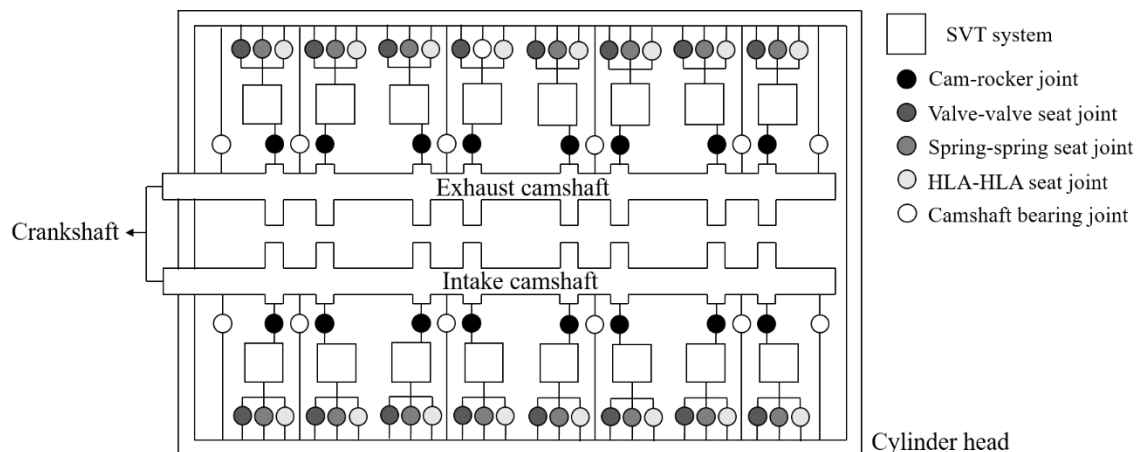


Figure 13. The topology of the valve train system.

Each single valve train (SVT) system model consists of a rocker, a hydraulic lash adjuster (HLA), a valve, and a valve spring, as shown in Figure 14. In each SVT system model, in addition to the joint connected to the camshaft, there are three joints connected to the cylinder head: valve–valve seat joint; valve spring–valve spring seat joint; and HLA–HLA seat joint. Each camshaft is connected to the cylinder head by six radial bearings and two thrust bearings (omitted in Figure 13). The front ends of the two camshafts are connected to the front end of the crankshaft, and the camshafts rotate at a speed of 1/2 of the crankshaft.

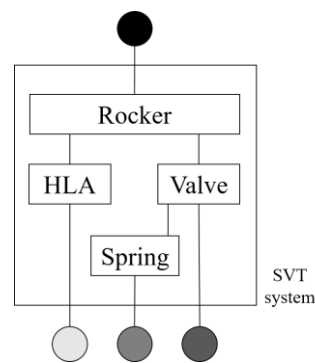


Figure 14. The topology of the SVT system.

The governing equations of motion are obtained for each element of the lumped masses through the Newton–Euler method and solved together in a time marching scheme [16]. In order to improve the accuracy of the model, the structure of the valve and the valve spring can be split into several discrete mass elements respectively, and the elements are connected in series by springs and dampers. Both the spring and the valve are limited to one-dimensional motion along the valve axis. The mass and stiffness of each discrete element of the spring are defined as [17]:

$$\begin{aligned} m_i &= 2\pi\rho A\Delta N_i r_i \\ \kappa_i &= \frac{I_i G_i \cos(\theta)}{2\pi r_i^3 \Delta N_i} \end{aligned} \quad (13)$$

where m is the mass, ρ is the density, A is the cross section area, ΔN is the discretized coil number, r is the radius of the discretized coil, κ is the stiffness, I is the torsional moment of inertia, G is the shear modulus, and θ is the pitch angle.

The rocker of the valve train is the roller finger follower type, which is mostly used in modern passenger cars, and has both rotational and translational DoFs. The overhead cam pushes the roller in the middle of the rocker, with the HLA as the pivot point, driving the valve to open and close. The deformation of the rocker has a great effect on the valve dynamic results. However, in uncoupled approaches, the components are generally simplified as rigid bodies connected by springs with constant stiffness, although the stiffness of the rocker arm varies continuously during the valve event [18]. In order to accurately simulate the rocker stiffness, the condensed rocker FEM model is adopted as shown in Figure 15. The rotational and translational DoFs of three nodes of the pivot point, the roller center, and the center of contact circle are retained.

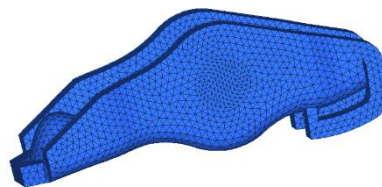


Figure 15. FEM model of the rocker.

A typical HLA, as shown in Figure 16, is used to maintain zero valve clearance, containing a plunger, outer housing, supply chamber, check valve, return spring, and high-pressure chamber (HPC). The lubricant flowing into the HPC is controlled by the check valve at the bottom of the plunger. The check valve is normally closed. After a certain amount of lubricant is lost, the check valve opens to refill the HPC. Due to the extension of the plunger, the valve clearance decreases. When the engine valve enters the lift phase, the check valve is closed, and the pressure in the oil chamber keeps the plunger in place and maintains an effective length to support the rocker [19].

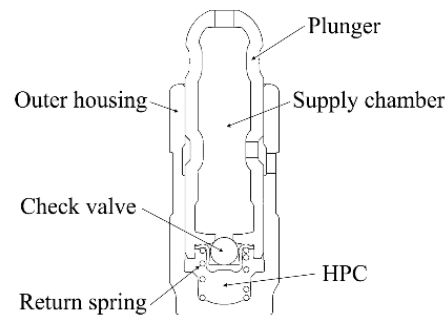


Figure 16. The structure of the hydraulic lash adjuster (HLA).

The lubricant pressure in the HPC is governed by the first order differential equation:

$$\frac{dP(t)}{dt} = \frac{\beta}{V(t)} \left(-\frac{dV(t)}{dt} + Q_{cv}(t) + Q_l(t) \right), \quad (14)$$

where β is the bulk modulus, V is the HPC volume, Q_{cv} is the volumetric flow through the check valve, and Q_l is the leakage through the clearance between the plunger and the outer housing.

The volumetric flow through the check valve can be obtained by:

$$Q_{cv} = \pm C_d S \sqrt{\frac{2|\Delta p|}{\rho}}, \quad (15)$$

where C_d is the discharge coefficient, S is cross-sectional area of the lubricant flow, ρ is the lubricant density, and Δp is the pressure difference between the HPC and the supply chamber.

The leakage through the clearance between the plunger and the outer housing can be obtained by:

$$Q_l = \pm \frac{\pi d \delta^3}{12\mu} \frac{|\Delta p|}{L}, \quad (16)$$

where d is the plunger diameter, δ is the radial clearance between the plunger and the outer housing, μ is the dynamic viscosity of the lubricant, and L is the leakage length.

3.5. Acoustic Model

Besides the classic methods of FEM and BEM (boundary element method), the Trefftz methods are applied in acoustic prediction. The wave-based technique (WBT) is an indirect and frameless Trefftz method [20]. Unlike the traditional element-based methods, WBT uses wave functions that exactly satisfy the governing dynamic equations but do not necessarily satisfy the boundary conditions [21]. The steady-state pressure p at position r is governed by the homogeneous Helmholtz equation.

$$\nabla^2 p(r) + k^2 p(r) = 0, \quad (17)$$

where ∇^2 is the Laplace operator, $k = \omega/c$ is the acoustic wave number, and c is the speed of sound.

As shown in Figure 17, the positions of sound level meters in the acoustic prediction model are arranged around the engine following ISO 3744-2010 [19], which is consistent with that in the measurements.

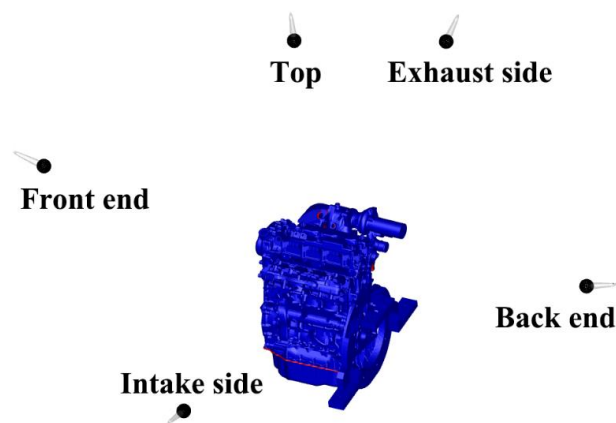


Figure 17. The positions of sound level meters in the acoustic prediction model.

4. Experimental Setup

Noise and vibration verification experiments of the engine are conducted with an AVL electric dynamometer of type 204/8 SL in a semi-anechoic room. The sound pressure level of background noise is below 25 dB(A) in the semi-anechoic room. As shown in Figure 18, five noise measuring points are arranged around the engine, following ISO 3744-2010. The distance between the microphones and the corresponding end faces of the engine is set to 1 m. Three vibration measuring points are arranged on the surface of the intake side of the cylinder head, as shown in Figure 19. All the microphones of type PCB 378B02 and acceleration sensors of type PCB 356A16 are connected to the LMS SCADAS data acquisition front-end after calibration. The signal acquisition and analysis software is LMS Test.Lab. The sampling frequency is 20,480 Hz, and the sampling time is 5 s. Measure twice and take the average value for each working condition. During the experiments, the water temperature was guaranteed to keep in a normal state, and the intake, exhaust, and coolant pipes were all properly led out, so the influences of external factors on the experiments were minimized.

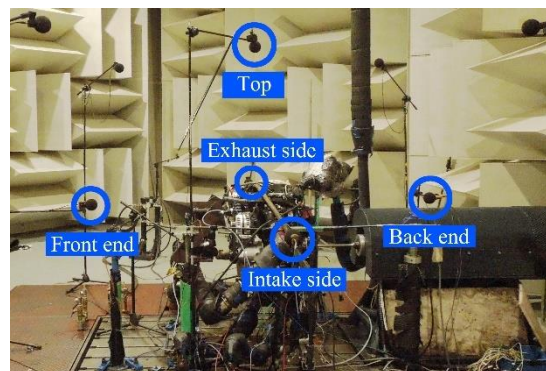


Figure 18. The positions of the microphones in the noise experiments.

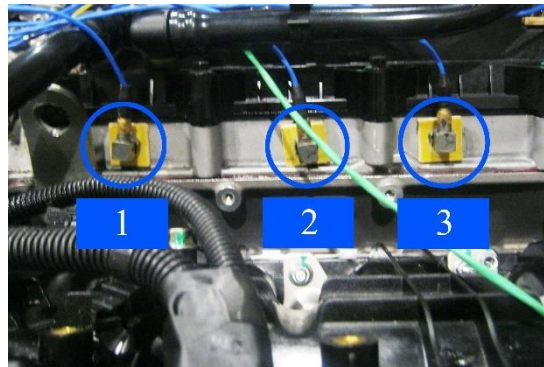


Figure 19. The positions of the acceleration sensors in the vibration experiments.

The sound pressure in pascals is measured. The A-weighted sound pressure level is expressed in decibels:

$$L_{pA} = 10 \lg \frac{p^2}{p_0^2}, \quad (18)$$

where the reference value $p_0 = 2 \times 10^{-5}$ Pa.

The A-weighted sound power level is expressed in decibels:

$$L_{WA} = 10 \lg \left[\frac{1}{N} \sum_{i=1}^N 10^{0.1 L_{pAi}} \right] + 10 \lg \left(\frac{S_1}{S_0} \right), \quad (19)$$

where N is the number of measuring points, L_{pAi} is the A-weighted sound pressure level at the i th measuring point, S_1 is the area of the measuring surface, and $S_0 = 1 \text{ m}^2$.

5. Results and Discussion

5.1. Valve Train Dynamic Analysis

It is a common approach to consider the forces from the valve train to the engine body as external loads, which can be called an uncoupled approach. Based on the uncoupled approaches, previous researchers performed dynamic simulations [9,22]. In this section, the dynamic analysis results using the coupled approach are compared with those in the uncoupled approach under the 2500 r/min WOT condition. The crank angles of 0 degree in the results are the moments of TDC on the compression stroke.

Figure 20 shows the exhaust valve displacement and velocity comparisons between the two approaches. It can be found from Figure 20a that the moments of valve opening, maximum lift, and closing are basically the same in the two approaches. Due to the vibration of the cylinder head, the displacement should fluctuate slightly after the closure of the exhaust valve. In the uncoupled approach, the valve is completely stationary when the valve is closed, since the valve train dynamic model is independent of the cylinder head, while the slight displacement fluctuation can be captured accurately in the coupled approach. A slight fluctuation in the valve velocity curves in the coupled approach in Figure 20b can also be observed. The zooming in views at the opening and closing sections of the exhaust valve velocity are shown in Figure 20c,d. Since the rotation speed fluctuation and the disturbance from the cylinder head are not taken into consideration in the uncoupled approach, the valve velocity curve is relatively smooth and idealized except for the moment of opening. In the coupled approach, there are some fluctuations throughout the valve opening section. In the valve closing section, the velocity curve in the coupled approach is also not as smooth as that in the uncoupled approach.

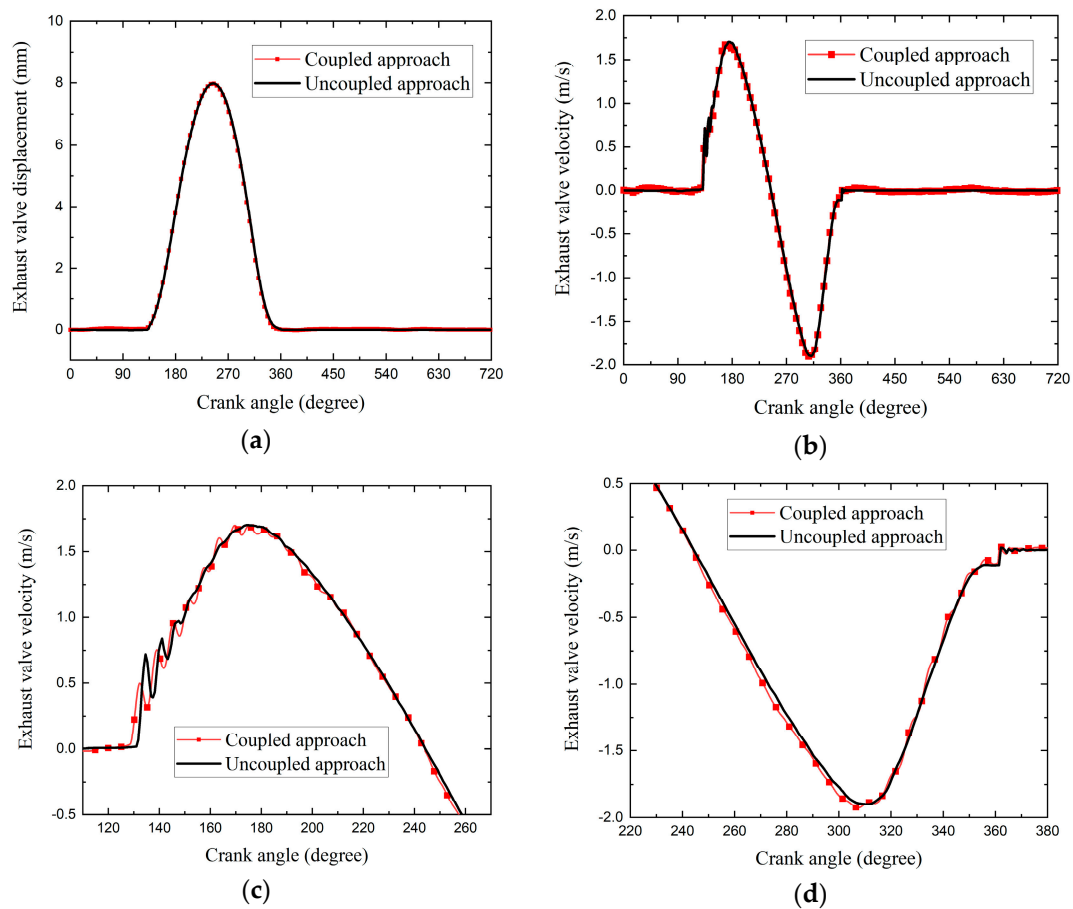


Figure 20. The exhaust valve displacement and velocity comparisons between the two approaches: (a) exhaust valve displacement; (b) exhaust valve velocity; (c) exhaust valve velocity (opening section); (d) exhaust valve velocity (closing section).

As shown in Figure 21, compared with the uncoupled approach, the acceleration curve of the coupled approach has a more obvious fluctuation, especially in the positive acceleration section. When the valve is seating, there is an acceleration peak of 4474 m/s² in the coupled approach and 5050 m/s² in the uncoupled approach.

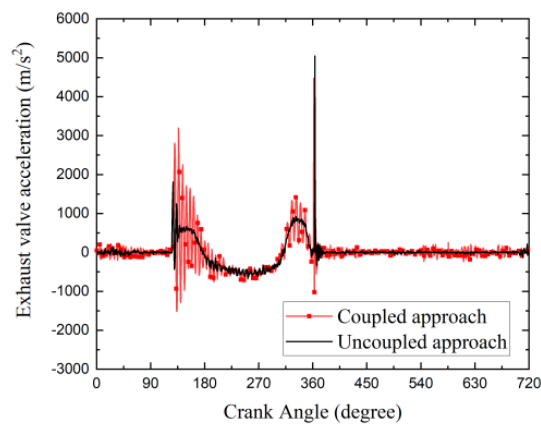


Figure 21. The exhaust valve acceleration comparison between the two approaches.

The impact force from the engine valve is an important source of excitation from the valve train system. The exhaust valve seating force comparison is shown in Figure 22. When the valve is

closed, the valve seat force is positively related to the in-cylinder pressure; therefore, the seat force curves of the two approaches are basically the same. When the valve is seated at the crank angle of 385 degrees, the peak force of the uncoupled approach is 412 N, while that of the coupled approach is 292 N. This shows that the flexible cylinder head model in the proposed approach may reduce the overestimated results of the valve seating force in the uncoupled approach.

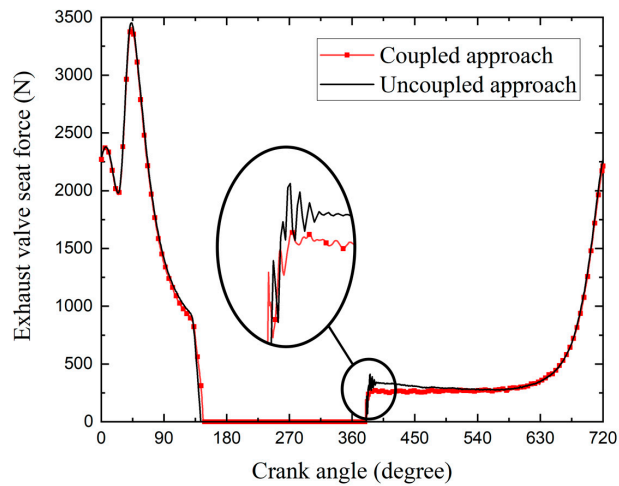


Figure 22. The exhaust valve seating force comparison between the two approaches.

The camshaft bearing force is another important source of excitation to the engine. The comparison of the camshaft bearing force in the Z-direction is shown in Figure 23. When the valve is opening, the peak force of the uncoupled approach is 2586 N, while that of the coupled approach is 3385 N. In the coupled approach, the camshaft bearing not only bears the force of the cam to open the valve, but also reflects the impact of the cylinder head vibration. Therefore, in the coupled approach, there are more fluctuations in the bearing force curve even when the valve is closed, compared with those in the uncoupled approach.

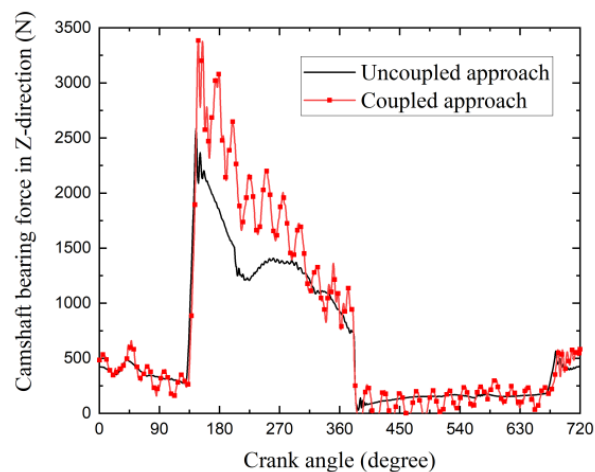


Figure 23. The camshaft bearing force in the Z-direction comparison between the two approaches.

When the valve is opening, the HLA as a pivot bears the force of the valve opening. The two curves have similar trends, as shown in Figure 24. Due to the HLA seat force of the coupled approach reflecting the vibration of the cylinder head, there are more fluctuations in the curve. The peak HLA seat force of the uncoupled approach is 651 N, while that of the coupled approach is 659 N.

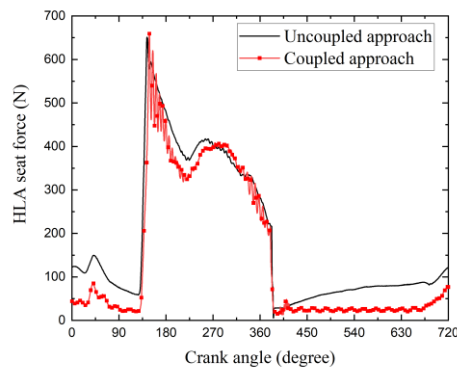


Figure 24. The HLA seat force comparison between the two approaches.

The force of the valve spring seat force is proportional to the valve lift. The preloads of the spring are 240 N. The trend of the two curves are basically the same as that shown in Figure 25. The curve of the coupled approach fluctuates more than that of the uncoupled approach, especially when the valves are opening and closing.

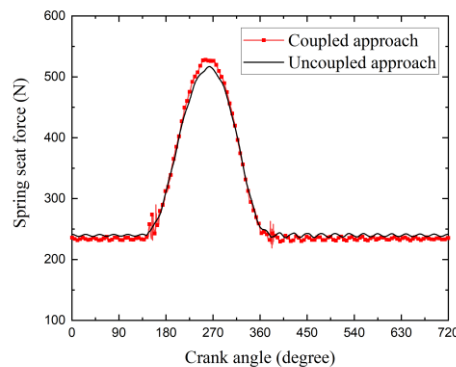


Figure 25. The spring force comparison between the two approaches.

Therefore, the above comparisons have verified that the results obtained by the proposed coupled approach are more reasonable than the uncoupled approach.

5.2. Vibration and Noise Results Analysis

In the experiment, the engine rotational speed is 2500 r/min, thus the fundamental frequency is 41.7 Hz. There are obvious peaks at the second (83.3 Hz), fourth (166.7 Hz), and sixth order (250.0 Hz) frequencies in both the vibration and sound spectrums. As shown in Figure 26, the 1/3 octaves of the measuring point 2 acceleration on the cylinder head vertical to the surface in two simulation approaches are compared with the measured value in the experiment. In the uncoupled approach, the amplitude of the 80 Hz center frequency band is 4.68 m/s^2 , which is much larger than the experimental value 1.43 m/s^2 . The amplitude at the second-order frequency of 83.3 Hz is significantly overestimated using the uncoupled approach. In the other frequency bands, the amplitude difference between the uncoupled approach and the coupled approach is relatively small, and there is not much difference with the experimental value. The amplitudes of the low frequency bands have a great influence on the overall value; therefore, the vibration acceleration is severely overestimated in the uncoupled approach.

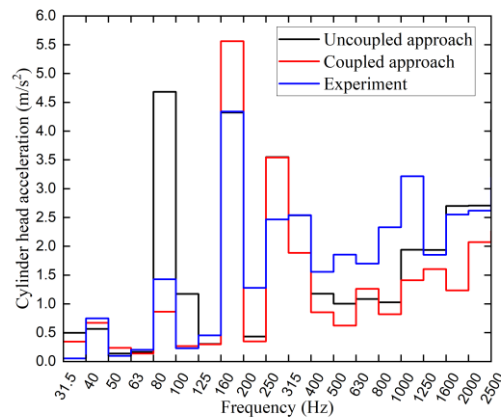


Figure 26. The 1/3 octave of measuring point 2 acceleration comparison between two approaches.

The vibration normal velocity level comparison colormaps between the two simulation approaches at the second order frequency of 83.3 Hz and the fourth order frequency of 166.7 Hz are shown in Figures 27 and 28, respectively. In order to show the velocity results of the cylinder head and the block more clearly, the intake manifold and the exhaust system are hidden in the colormaps, while in fact they are also involved in the calculation of vibration and noise.

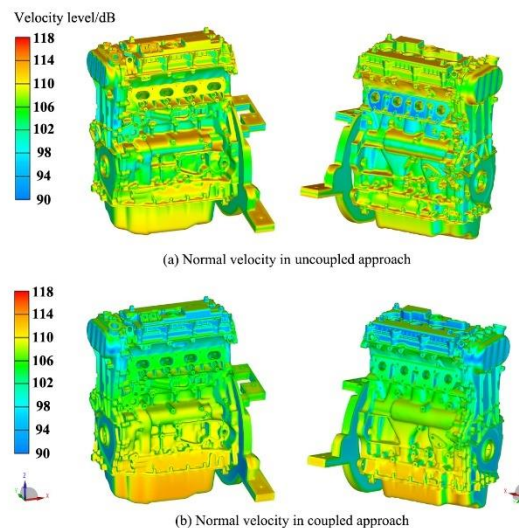


Figure 27. The colormaps of the vibration normal velocity level comparison between the two approaches at the frequency of 83.3 Hz.

The velocity levels at the second order frequency of 83.3 Hz are where the two approaches differ most. As shown in Figure 27, the normal velocity levels of the upper parts of the engine including the cylinder head and the cylinder head cover in the uncoupled approach are larger than those in the coupled approach. This is consistent with the previous conclusion that the uncoupled approach overestimates the second-order vibration. The velocity levels at the fourth order frequency of 166.7 Hz are relatively close between the two approaches, as shown in Figure 28. In the coupled approach, the vibration velocities of the cylinder head and the block are slightly higher than those in the uncoupled approach, which is consistent with the previous 1/3 octave acceleration results on the cylinder head.

The comparison of the acoustic results shows similar trends, as shown in Figure 29. The sound pressure level at the top measuring point at the second order frequency is 63.6 dB(A) in the uncoupled approach, which is significantly overestimated compared with the experimental value 52.1 dB(A). The coupled approach value is 56.6 dB(A), which is much closer to the experimental value. The coupled approach has a higher accuracy at the fourth order frequency. The coupled approach value is 59.5 dB(A),

and the difference from the experimental value 60.4 dB(A) is only 0.9 dB(A). The uncoupled approach value is 54.8 dB(A), and the difference from the experimental value is 5.6 dB(A). At the sixth order frequency of 250 Hz, the coupled approach value also has a better precision. The measured value is 52.4 dB(A), and the value of the coupled approach is 57.7 dB(A), while the value of the uncoupled approach is 61.1 dB(A). The coupled approach shows a better accuracy on noise prediction in the lower frequency bands, which has a great impact on the overall sound pressure level value.

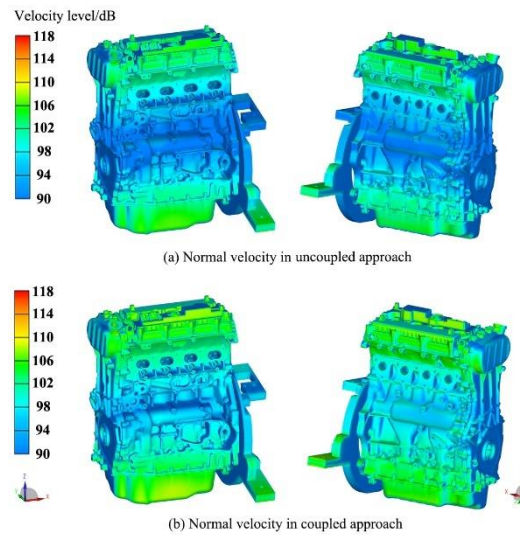


Figure 28. The colormaps of the vibration normal velocity level comparisons between the two approaches at the frequency of 166.7 Hz.

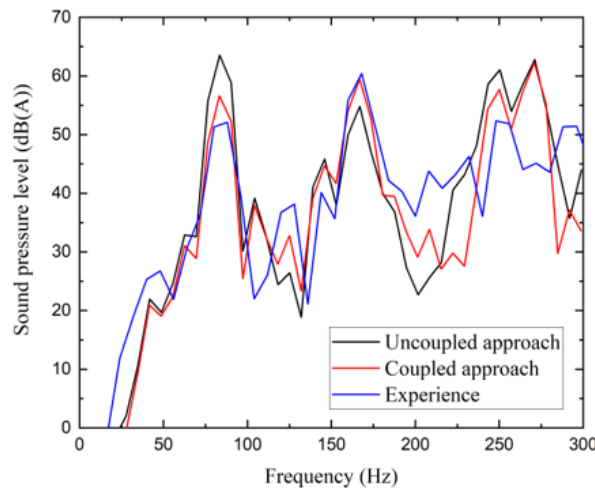


Figure 29. The sound pressure level at the top measuring point in the frequency domain comparison between the two approaches.

The sound pressure level comparisons of the five measuring points between the two simulation approaches and the experimental values are shown in Figure 30. Both two simulation results of all the measuring points are larger than the experimental values, except for the intake side measuring point. It can be inferred that the predicted noise values at the intake side measuring point are relatively underestimated because the engine models ignore high-pressure oil pumps and rails, the filter bases, and some front-end accessories (alternators and air-conditioning compressors). Compared with the uncoupled approach, the results in the coupled approach have a better accuracy at most measuring points, as shown in Figure 31.

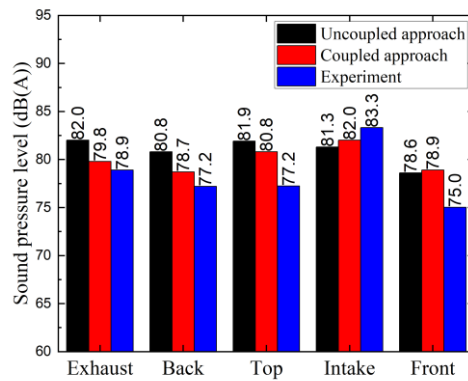


Figure 30. The sound pressure level comparisons of the five measuring points between the two simulation approaches and the measurements.

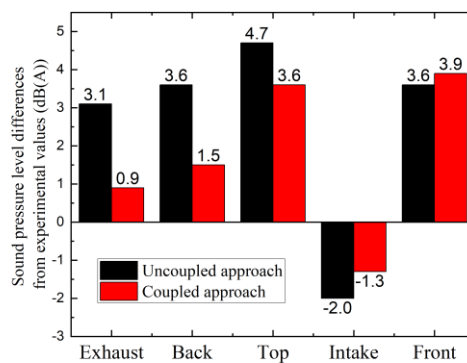


Figure 31. The sound pressure level differences of the two simulation approaches from the experimental values.

The overall sound power level comparison is shown in Figure 32. The simulation results in the uncoupled approach and the coupled approach are 95.4 dB(A) and 94.5 dB(A), respectively, while the experimental value is 93.6 dB(A). After using the coupled approach, the difference from the experiment is reduced from 1.8 dB(A) to 0.9 dB(A). The analyses show that the vibration and noise results obtained by the proposed coupled approach are closer to the experimental value.

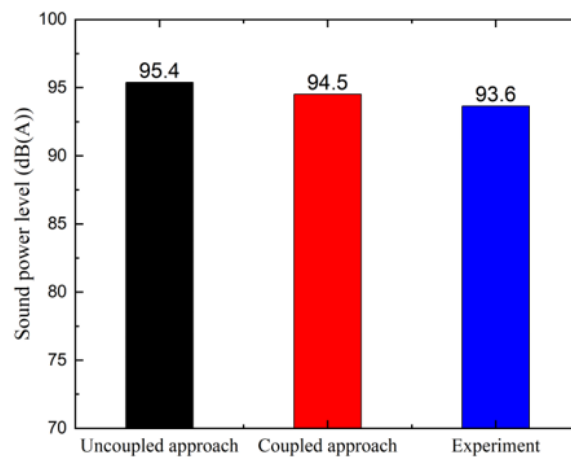


Figure 32. The overall sound power level comparison between the two simulation approaches and the experimental value.

6. Conclusions

A completed coupled engine dynamic model with the valve train system is proposed. The valve train system is integrated into the engine model, forming the full engine dynamic model. Based on the coupled multi-body dynamic model, the dynamic simulation is performed and the vibration and noise are predicted. The results of the coupled approach are compared with those of the uncoupled approach and the experimental values. The conclusions are summarized as follows:

1. The coupled approach considers interaction ignored in the uncoupled approach, which can improve the fidelity of the model. The impact of the cylinder head deformation to the valve train and the support and constraints of the valve train on the cylinder head are taken into consideration in the coupled approach. The camshaft speed is obtained from the crankshaft speed in the simulation, instead of a constant or preset speed. Therefore, the influence of speed fluctuation on the valve train is taken into consideration as well.
2. Applying the coupled approach, more detailed dynamic results of the valve train are presented. The influence of the interaction between the valve train system and the cylinder head can be observed in the simulation results of the parts displacements, velocities, accelerations, and forces. The coupled approach is more instructive for analyzing the fatigue problems and abnormal noise problems of the valve train system.
3. Compared with the uncoupled approach, the results of the coupled approach have a better accuracy in vibration simulations. The vibration of the cylinder head measuring point at the second-order frequency (83.3 Hz) is severely overestimated in the uncoupled approach, resulting in the overestimation of the overall vibration and noise. In the coupled approach, the results of vibration at the second-order frequency are closer to the experimental values.
4. The coupled approach has a better accuracy in noise prediction as well. The calculated overall sound power level values in the uncoupled and coupled approaches are 95.4 dB(A) and 94.5 dB(A), respectively, while the experimental value is 93.6 dB(A). After using the coupled approach, the difference from the experimental value is reduced from 1.8 dB(A) to 0.9 dB(A).

Author Contributions: For this research, X.Z. and X.L. put forward the approaches and established the simulation models; Y.Q. and Z.H. provided the experiment support; X.Z. and X.L. wrote the paper; while Y.Q. and Z.H. further improved the manuscript. All authors have read and agreed to the published version of the manuscript.

Funding: This research was funded by the National Natural Science Foundation of China grant number 51876188 and 51705454 and the National Key Research and Development Program of China grant number 2016YFB0101604.

Conflicts of Interest: The authors declare no conflict of interest.

References

1. Dudley, W.M. New method in valve cam design. *SAE Tech. Pap.* **1948**, 480170. [[CrossRef](#)]
2. Eiss, N.S., Jr. Vibration of cams having two degrees of freedom. *J. Eng. Ind.* **1964**, *86*, 343–349. [[CrossRef](#)]
3. Chan, C. Dynamic model of a fluctuating rocker-arm ratio cam system. *J. Mech. Des.* **1987**, *109*, 356–365. [[CrossRef](#)]
4. Seidlitz, S. Valve train dynamics—a computer study. *SAE Tech. Pap.* **1989**, 890620. [[CrossRef](#)]
5. Nagaya, K. Vibration analysis of high rigidity driven valve system of internal combustion engines. *J. Sound Vib.* **1993**, *165*, 31–43. [[CrossRef](#)]
6. Pisano, A.P. An experimental and analytical investigation of the dynamic response of a high-speed cam-follower system. *J. Mech. Transm. Autom. Des.* **1983**, *105*, 699–704. [[CrossRef](#)]
7. Lassaad, W. Nonlinear dynamic behaviour of a cam mechanism with oscillating roller follower in presence of profile error. *Front. Mech. Eng.* **2013**, *8*, 127–136. [[CrossRef](#)]
8. Guo, J. A new numerical method for developing the lumped dynamic model of valve train. *J. Eng. Gas Turbines Power* **2015**, *137*, 101507. [[CrossRef](#)]
9. Zhou, C. An enhanced flexible dynamic model and experimental verification for a valve train with clearance and multi-directional deformations. *J. Sound Vib.* **2017**, *410*, 249–268. [[CrossRef](#)]

10. Meuter, M. Multi-Body engine simulation including elasto-hydrodynamic lubrication for non-conformal conjunctions. *Proc. Inst. Mech. Eng. Part K J. Multi-Body Dyn.* **2017**, *231*, 457–468. [CrossRef]
11. Offner, G. Modelling of condensed flexible bodies considering non-linear inertia effects resulting from gross motions. *Proc. Inst. Mech. Eng. Part K J. Multi-Body Dyn.* **2011**, *225*, 204–219. [CrossRef]
12. Angeles, J.; Zakhariiev, E. *Computational Methods in Mechanical Systems: Mechanism Analysis, Synthesis, and Optimization*; Springer: Berlin/Heidelberg, Germany, 1998.
13. Morrison, D. A framework for modal synthesis. *Comput. Music J.* **1998**, *17*, 45–56. [CrossRef]
14. Craig, R.R., Jr.; Bampton, M.C.C. Coupling of substructures for dynamic analyses. *AIAA J.* **1968**, *6*, 1313–1322. [CrossRef]
15. Liu, R. A study of the influence of cooling water on the structural modes and vibro-acoustic characteristics of a gasoline engine. *Appl. Acoust.* **2016**, *104*, 42–49. [CrossRef]
16. Teodorescu, M. Multi-Physics analysis of valve train systems: From system level to microscale interactions. *Proc. Inst. Mech. Eng. Part K J. Multi-Body Dyn.* **2007**, *221*. [CrossRef]
17. Haslinger, J. Non-Smooth dynamics of coil contact in valve springs. *J. Appl. Math. Mech.* **2014**, *94*, 957–967. [CrossRef]
18. Beloiu, D.M. Modeling and analysis of valve train, part I-conventional systems. *SAE Int. J. Engines* **2010**, *3*, 850–877. [CrossRef]
19. ISO. *Acoustics—Determination of Sound Power Levels and Sound Energy Levels of Noise Sources Using Sound Pressure—Engineering Methods for an Essentially Free Field Over a Reflecting Plane*; International Organization Standardization: Geneva, Switzerland, 2010; Volume 3744.
20. Desmet, W. A Wave Based Prediction Technique for Coupled Vibro-Acoustic Analysis. Ph.D. Thesis, Katholieke Universiteit Leuven, Leuven, Belgium, 1998.
21. AVL Workspace. Excite-Power-Unit Theory: AVL User Manuals. 2017. Available online: <http://www.avl-ast-china.com/upload/ueditor/file/20170516/1494905319788032969.pdf> (accessed on 24 July 2020).
22. Andreatta, E.C. Valve train kinematics and dynamics simulation. *SAE Tech. Pap.* **2016**, *36*, 0213. [CrossRef]



© 2020 by the authors. Licensee MDPI, Basel, Switzerland. This article is an open access article distributed under the terms and conditions of the Creative Commons Attribution (CC BY) license (<http://creativecommons.org/licenses/by/4.0/>).